A Plasma Torus Around a Young Low-Mass Star

Luke G. Bouma[1, 2, *]

[1]*Observatories of the Carnegie Institution for Science, Pasadena, CA 91101, USA*
[2]*Department of Astronomy, California Institute of Technology, Pasadena, CA 91125, USA*

ABSTRACT

A small fraction of red dwarfs younger than $\sim$100 million years show structured, periodic optical light curves suggestive of transiting opaque material that corotates with the star. However, the composition, origin, and even the existence of this material are uncertain. The main alternative hypothesis is that these complex periodic variables (CPVs) are explained by complex distributions of bright or dark regions on the stellar surfaces. Here, we present time-series spectroscopy and photometry of a rapidly-rotating (P=3.9 hr) CPV, TIC 141146667. The spectra show sinusoidal time-varying Hα emission at twice to four times the star's equatorial velocity, providing direct evidence for cool ($\lesssim$10^4 K) plasma clumps trapped in corotation around a CPV. These data support the idea that young, rapidly-rotating M dwarfs can sustain warped plasma tori, similar to massive magnetic stars. It remains unclear whether these structures originate intrinsically from the star or are fed by external sources. Likewise, the mechanism by which their optically thick clumps arise is still unknown. Rough estimates suggest $\gtrsim$10% of M dwarfs host similar structures during their early lives.

1. INTRODUCTION

Stars with masses below about half that of the Sun, M dwarfs, are the only type of star to offer near-term prospects for detecting the atmospheres of rocky exoplanets with surface water. Community investment with JWST is proceeding accordingly (Redfield et al. 2024; TRAPPIST-1 JWST Community Initiative et al. 2024). The question of how M dwarfs influence their planets—especially the retention of their atmospheres—has correspondingly grown in importance. Previous work has established that most M dwarfs host close-in planets (Dressing & Charbonneau 2015) that on average are subject to long circumstellar disk lifetimes (Ribas et al. 2015), to high doses of UV radiation (France et al. 2016), and to a high incidence of flares and coronal mass ejections (Feinstein et al. 2020). However, despite extensive work in these areas, the plasma and magnetospheric environments that bathe young, close-in exoplanets remain challenging to quantify. Understanding these environments is crucial because they directly impact atmospheric retention and habitability of close-in exoplanets.

One example of our current ignorance is the complex periodic variables. While Figure 1 highlights the main object of interest in this article, over one hundred analogous systems have now been found by K2 and TESS (Rebull et al. 2016; Stauffer et al. 2017; Rebull et al. 2018; Zhan et al. 2019; Rebull et al. 2020; Stauffer et al. 2021; Popinchalk et al. 2023; Bouma et al. 2024). These CPVs are phenomenologically identified based on their structured, periodic optical light curves; most are M dwarfs with rotation periods shorter than two days. Within current sensitivity limits, none host disks (Stauffer et al. 2017; Bouma et al. 2024). However, $\approx$3% of stars a few million years old show this complex behavior, an observed fraction which decreases to $\approx$0.3% by $\approx$110 Myr (Rebull et al. 2020). CPVs can and have been confused for transiting exoplanets (van Eyken et al. 2012; Johns-Krull et al. 2016; Bouma et al. 2020).

The two leading hypotheses for explaining CPVs are either that transiting clumps of circumstellar material corotate with the star (Stauffer et al. 2017; Günther et al. 2022; Bouma et al. 2024), or that these stars represent an extreme in naturally-occurring distributions of starspots or faculae (Koen 2021). The main argument against a starspot-only explanation invokes the timescales and amplitudes of the sharpest photometric features. However, no independent evidence has yet been acquired for the presence of any circumstellar material. If such material exists, then the geometric correction from the transit probability would imply an intrinsic occurrence rate at least a few times larger than the observed rate, suggesting that these clumps could exist around $\gtrsim$10% of M dwarfs during their early lives.

The dearth of evidence for circumstellar material around CPVs is surprising given that separate studies of young stars have, for decades, reported that stellar coronae contain both

Corresponding author: Luke G. Bouma

* Carnegie Fellow; 51 Pegasi b Fellow

2022-02-16 - 2022-02-17
Cycle 1265 - 1268, Sector 48

Figure 1 (Movie). TIC 141146667 is a complex periodic variable (CPV). The online movie, **available here**, covers a baseline of 5,784 cycles irregularly sampled over three years. The TESS light curve is phased to the 3.930 hour period in groups of three cycles per frame. This is the period both of stellar rotation, and (we hypothesize) of corotating clumps of circumstellar material. Raw data acquired at two minute dence are in gray; black averages to 100 points per cycle. The sharp photometric features persist for tens to thousands of rotational cycles.

hot ($\gtrsim 10^6$ K) and cool ($\lesssim 10^4$ K) plasma. In particular, time-series spectroscopy of stars with a wide range of masses has shown periodic high-velocity absorption and emission in Balmer lines such as Hα, interpreted as long-lived, corotating clumps of cool plasma (Collier Cameron & Robinson 1989; Collier Cameron & Woods 1992; Barnes et al. 2000; Donati et al. 2000; Dunstone et al. 2006; Skelly et al. 2008; Leitzinger et al. 2016; Cang et al. 2021). Such clumps are thought to be forced into corotation by the star's magnetic field, and the exact geometry of where the plasma can accumulate is dictated by the field's topology. For instance, a magnetic dipole field tilted with respect to the stellar spin axis yields accumulations in a warped torus geometry (Townsend & Owocki 2005), whereas in the limit of a single strong field line, accumulation occurs at the line's apex, furthest from the star (Waugh & Jardine 2022). To date, none of these spectroscopic variables have shown any photometric anomalies (Bouma et al. 2024), leaving open the issue of whether they are related to CPVs.

In this study, we present the first spectroscopic detection of corotating clumps of cool plasma around a CPV, TIC 141146667. Section 2 describes our observations; Section 3 presents the results; Section 4 discusses their interpretation and highlights future directions.

Table 1. Selected system parameters for TIC 141146667.

Parameter	Description	Value	Source
$T_{\rm eff}$	Effective Temperature (K) . . .	2972 ± 40	1
$R_\star$	Stellar radius ($R_\odot$)	0.42 ± 0.02	1
Age	Stellar age range (Myr)	35-150	2
$M_\star$	Stellar mass ($M_\odot$)	0.22 ± 0.02	3
γ	Systemic radial velocity (km s^{-1})	0.61 ± 1.47	4
SpT	Spectral Type	M5.5Ve	4
$P_{\rm rot}$	Photometric rotation period (hr)	3.930 ± 0.001	5
$v_{\rm eq}$	Equatorial velocity	130 ± 4	6
	$(2\pi R_\star / P_{\rm rot})$ (km s^{-1})		
$v_{\rm eq} \sin i_\star$.	Projected rotational	138 ± 8	4
	velocity (km s^{-1})		
$v_{\rm break}$	Breakup velocity	316 ± 16	6
	$(GM_\star / R_\star)^{1/2}$ (km s^{-1})		
$i_\star$	Stellar inclination	>63	4
	2σ lower limit (deg)		
d	Distance (pc)	57.54 ± 0.09	7
$R_{\rm c}$	Keplerian corotation	1.82 ± 0.10	6
	radius ($R_\star$)		
a_0	Mean inner clump (0)	2.07 ± 0.04	4
	orbital radius ($R_\star$)		
a_1	Mean inner clump (1)	2.88 ± 0.10	4
	orbital radius ($R_\star$)		
a_2	Mean outer clump	3.88 ± 0.25	4
	orbital radius ($R_\star$)		
$\langle {\rm EW}_{\rm H\alpha} \rangle$	Time-averaged Hα line core	7.2 ± 0.2	4
	equivalent width (Å)		

NOTE— Provenances are: 1: SED fit (Bouma et al. 2024). 2: Gaia DR3 photometry shows the star is on the pre-main sequence, while the spectrum lacks lithium (Appendix A). 3: PARSEC v1.2S (Chen et al. 2014). 4: Keck/HIRES (Appendix B). 5: TESS light curve. 6: Derived quantity. 7: Gaia DR3 geometric (Gaia Collaboration et al. 2023).

2. OBSERVATIONS

We identified TIC 141146667 in previous work (Bouma et al. 2024) by searching TESS two-minute data from 2018-2022 for highly structured, periodic light curves (Ricker et al. 2015). We chose the star for spectroscopy because its brightness and rapid rotation enabled an efficient search for variability in its line profiles. As an apparently single pre-main sequence M dwarf, its properties are typical for the CPV population (see Table 1 and Appendix A).

We observed TIC 141146667 (V=16.2) for five hours on 17 February 2024 using the High Resolution Echelle Spectrometer (HIRES; Vogt et al. 1994) on the 10 m Keck I telescope. The observations spanned the second half of the night, from 17 February 2024 10:47 to 16:13 (UT). The star's airmass spanned z=1.2-2.2, and we opted for a fixed 15 minute
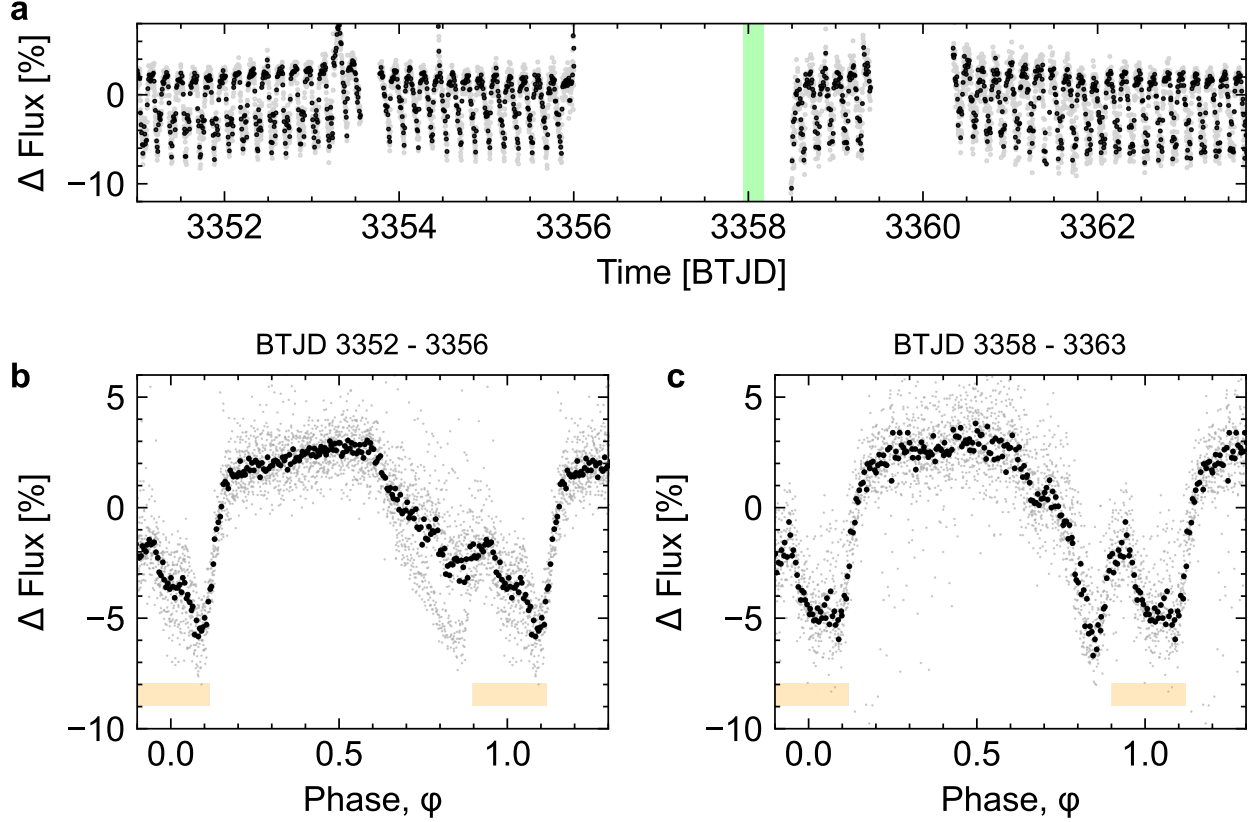
Figure 2. Evolution of TIC 141146667 during the Keck/HIRES observation (green bar). a, TESS simple aperture photometry. Data gaps caused by light from Earth (BTJD 3356-3358.5) and Moon (BTJD 3359.5-3360.5) are visible. Raw two minute data are in gray; black time-averages to ten minute sampling. **b-c,** Folded TESS light curve before and after spectroscopy. Black now phase-averages to 100 points per cycle. During BTJD 3352-3356, a state switch occurred near BTJD 3353, and the dip at $\phi{\approx}0.8$ disappeared. While the large flux decrement was present both before and after the HIRES sequence, its photometric shape evolved during the data gap. The orange bar denotes times of spectroscopic transits for the inner two Hα clumps observed with HIRES (see Figure 3).

cadence, except for a final 10 minute exposure due to increasing sky brightness at sunrise. We observed without the iodine cell and used the C2 decker ($0\rlap{.}''86 \times 14\rlap{.}''0$) in the red configuration, yielding a spectral resolution $R{\approx}45{,}000$ ($\delta v{\approx}6.7\,\mathrm{km\,s^{-1}}$; $\delta v/v_{\mathrm{eq}}{\approx}0.05$). We binned the CCD readout by a factor of three in the spatial dimension, yielding ${\approx}1{,}000$ photons (S/N=33) per pixel in the continuum at 6500 Å, at minimum airmass. Strong winds contributed to $1''\text{-}1\rlap{.}''5$ seeing over the night, but conditions were otherwise favorable. We reduced the echelleogram to a one-dimensional spectrum using the standard techniques of the California Planet Survey (Howard et al. 2010).

TESS observed TIC 141146667 (T=13.3) for six non-contiguous months spanning 2019-2024. TESS acquired these observations at two-minute cadence during Sectors 41, 48 (TESS DDT039, PI: Kunimoto), and 75 (TESS Program G06030, PI: Bouma). The 30-minute data during Sectors 14, 15, and 21 probably smeared sharp features over the star's 3.93 hour period (see Günther et al. 2022). The movie in Figure 1 shows the two-minute data: like other CPVs, TIC 141146667 maintains a fixed period over timescales of years while its detailed photometric morphology evolves.

The nearest known star, TIC 141146666 (T=14.5), is $25''$ from TIC 141146667 and is photometrically stable in the TESS images; crowding is not a concern.

We observed with Keck during Sector 75 in an attempt to obtain simultaneous observations. Figure 2 shows the result; Earth passed within $25°$ of the TESS camera's boresight from BTJD 3356.0-3358.5, which caused a data gap that ended twelve hours after our Keck/HIRES observations (green bar). From BTJD 3359.4-3362.0, the Moon then passed within $25°$ of the camera's boresight. Based on the level of scattered light in the optimal TIC 141146667 aperture (Jenkins et al. 2016), we manually masked out data in the TESS light curve from 3359.40-3360.13; the remainder of the data during the lunar approach were usable. Small gaps from BTJD 3353.55-3353.77 and 3360.12-3360.33 were caused by data downlinks at the spacecraft's perigee and apogee.

Although the data gap is unfortunate, Figure 2 shows that both before and after the HIRES data were acquired, a large flux decrement spanned roughly half of each cycle. From BTJD 3352-3356, this dip had two sharp local minima; the minimum at $\phi{\approx}0.8$ decreased in depth following the flare at BTJD 3353, yielding a dip more closely resembling an
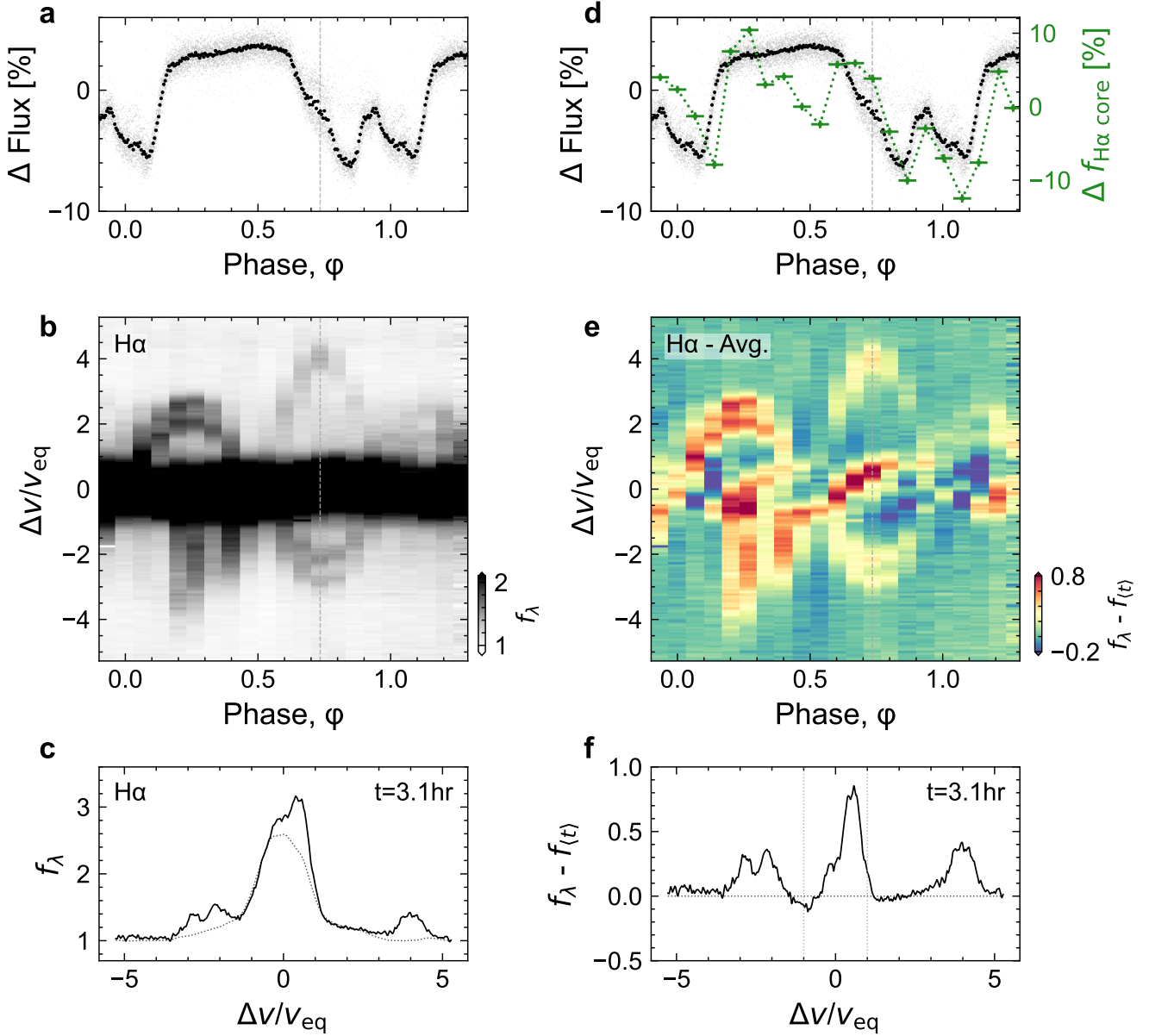
Figure 3 (Movie). Emission from circumstellar plasma orbiting TIC 141146667. The online movie, **available here**, shows the spectral evolution over five hours. **a,** Average TESS light curve from 5 February 2024 to 26 February 2024 folded on the 3.930 hour period. Black points are phase-averaged; gray are the raw data. **b,** Keck/HIRES Hα spectra acquired on 17 February 2024. The continuum is set to unity, and the darkest color is at twice the continuum to accentuate emission outside the line core ($|v/v_{eq}| > 1$, for $v_{eq}=130\,\mathrm{km\,s^{-1}}$). While emission in the line core originates in the star's chromosphere, the sinusoidal emission features are most readily described by a warped plasma torus. **c,** Individual epochs of Panel b, visible in the online movie. The dotted line shows the time-averaged spectrum, $f_{\langle t \rangle}$. **d,** As in Panel a, but overplotting the median-normalized Hα light curve at $|v/v_{eq}| < 1$. **e,** As in Panel b, after subtracting the time-averaged spectrum. The line core shows Hα excesses and decrements advancing from the blue to red wings. The asymmetric color stretch is set to mirror the dynamic range of the data. **f,** Individual epochs of Panel e, visible in the online movie.

asymmetric "V" than a "W". Similar CPV state changes have been previously noted (Stauffer et al. 2017; Bouma et al. 2024). The photometric shape therefore evolved during the twelve cycles spanning the 3356-3358 gap, since the average shape from 3358-3363 more closely resembles the initial "W". Nonetheless, the general photometric morphology—a small brightening over 45% of the period, followed by a complex flux dip spanning 55% of the period—is similar before and after the data gap.

3. RESULTS

Figure 3 compiles the TESS and HIRES data from February 2024. The HIRES spectra show emission in Hα beyond

the star's equatorial velocity, v_{eq}, of $130\,\mathrm{km\,s^{-1}}$. There are at least two distinct emission components, separated by $180°$ in phase. The inner component at lower velocities has clearer sinusoidal behaviour in time and is double-peaked, with peak semi-amplitudes of $2.07\,v_{eq}$ and $2.88\,v_{eq}$, measured following the procedure in Appendix B. There is significant non-periodic variability in the emissivity of this double-peaked component: the flux excess begins with an amplitude 70% that of the continuum, and diminishes to 10% by the end. The higher-velocity component $180°$ opposite in phase is detected only from ϕ=0.2-1.0. From ϕ=0.2-0.5, this outer component appears connected to the star in velocity space. While its peak semi-amplitude of $3.88\,v_{eq}$ is achieved at both ϕ=0.25 and 0.75, its amplitude similarly decreases from a 60% excess over the continuum at the beginning of the observation sequence to a 10% excess by its end. From the same procedure in Appendix B, we measured the period for all three spectroscopic emission components to be consistent with the photometric 3.930 hour period, to within two minutes for the lower-velocity component.

These sinusoidal emission features require circumstellar clumps of partially-ionized hydrogen to corotate with the star. Based on the observed sinusoidal periods and velocities, this material's motion is not controlled by gravitational attraction to the star; it is a plasma being dragged along with a rigidly rotating stellar magnetic field. The velocity semi-amplitude of the sinusoids gives the mean distance of each clump from the stellar surface: $2.07\,R_\star$ and $2.88\,R_\star$ for the inner clumps, and $3.88\,R_\star$ for the outer clump. These clumps transit in front of the star when passing from negative to positive velocity. The transits of the two inner clumps last $\approx$22% of each cycle, from ϕ=-0.1 to ϕ=+0.12 (see Appendix B). This spectroscopic transit coincides with the latter half of the complex eclipse feature in the TESS data.

The Hα line core is more complex. At $|\Delta v/v_{eq}| < 1$, most observed Hα photons come from the star's chromosphere; circumstellar material might also modulate the line profile. Figure 3e suggests line core variability caused by both bright and dark regions on the star's surface, superposed with smaller-amplitude variability from the transiting circumstellar material. For instance, from ϕ=0-0.3, the double-peaked emission feature is visible when viewed both on and off-limb; this feature is circumstellar in origin. However, the large emission feature that crosses the star from ϕ=0.4-0.9 emits at an amplitude greater than that observed from the circumstellar components, and it crosses the stellar velocity surface at a speed that suggests it instead originates from a chromospherically bright region on the star's surface. Similarly, from ϕ=0.6-1.15 a 20% deep absorption feature slowly crosses the Hα line profile. This feature suggests either a chromospherically dark region (e.g. a starspot group) crossing the star's surface, or an azimuthally extended absorptive component to the circumstellar material which is not visible in emission. While the origin of the other bright and dark streaks passing across the line core are similarly ambiguous, a final exercise to quantify the behavior of the line core is shown in Figure 3d, where $f_{\mathrm{H}\alpha\,\mathrm{core}}$ denotes the summed flux at $|\Delta v/v_{eq}| < 1$. This panel shows that changes in the line core flux correlate with the broadband variability throughout most of the light curve, except near ϕ≈0.5, corresponding to the transit of the $3.9\,R_\star$ clump and the occultation of the lower-velocity clump.

4. DISCUSSION

4.1. *Physical Properties of the Emitting Region*

Our Keck/HIRES observations are the first reported time-series spectra of a CPV, and they demonstrate that corotating circumstellar plasma clumps exist around at least one such star. More specifically, the spectra require plasma with a significant population of hydrogen in the n=3 excited state, with minimal evidence for higher-order excitations (see Appendix C). Most of this Hα emission originates in "clumps" with size comparable to the star; radial "spokes" or azimuthally-extended "arcs" for the emitting material are ruled out by the $\approx$30 km s^{-1} Hα velocity dispersion (see Appendix B). The Hα line luminosity suggests characteristic number densities and masses for the gaseous component of these clumps of $n_{\mathrm{H}} \sim 10^{11}$ cm^{-3} and $M_{\mathrm{gas}} \sim 10^{17}$ g (see Appendix D). Dust is independently constrained to have a total mass $M_{\mathrm{dust}} < 10^{17}$ g based on the lack of a WISE infrared excess; if one assumes that the opacity in the TESS flux dips comes from dust, a lower limit $M_{\mathrm{dust}} > 10^{15}$ g follows (see Appendix E).

4.2. *Clumps Within Warped Plasma Torii*

While the Hα emission seems to mostly originate from clumps, the complex flux dip in TIC 141146667 spans roughly half of each cycle; in CPVs more broadly, individual dips can last 5-50% of each cycle, and they are often distributed in longitude (Bouma et al. 2024). This raises the possibility that azimuthally-distributed material may be the norm for CPVs, and that a warped torus may be a more accurate picture than a clump.

Townsend & Owocki (2005) outlined the physics of how rapidly-rotating stars with strong magnetic fields can support plasma tori. When the magnetospheric radii R_{m} of such stars exceeds their Keplerian corotation radii R_{c}, the effective potential experienced by charged particles has a local minimum outside R_{c}, which enables charged material to accumulate in a torus (Petit et al. 2013; Daley-Yates & Jardine 2024). Warps can occur when there is misalignment between the spin and magnetic axes. In general, the material in these centrifugally-supported magnetospheres need neither transit nor be opaque in broadband optical light.

In a follow-up study, Townsend (2008) synthesized light curves for these systems, assuming that the optical depth scaled linearly with density. They found that W-shaped eclipses, similar to those seen for TIC 141146667, can occur when the spin and magnetic axes are moderately (15-45°) misaligned. The movies associated with their work

are available online[‡]; for a $\omega/\omega_c \approx 0.5$, edge-on system like TIC 141146667, the photometric eclipses have the correct shape, and the Hα emission similarly exhibits double-peaked behavior. The plasma in this model accumulates at antipodes 180° apart because the deepest local minima in the effective potential exist along the line of intersection between the rotational and magnetic planes (see Equation 22 of Townsend & Owocki 2005).

To summarize, the lines of evidence in favor of warped plasma tori for TIC 141146667 and CPVs more generally are that *i)* Figure 3 shows two emitting plasma clumps separated 180° in phase, with double-peaked Hα morphology at quadrature; *ii)* the "W" shaped photometric eclipses are predictions of such a model; *iii)* CPV dips last 5-50% of each cycle, suggesting an extended azimuthal distribution of circumstellar material.

4.3. *Origin of CPV Photometric Variability and Astrophysical Analogs*

Microphysically, it is not obvious whether hydrogen alone can produce the broadband chromatic flux variations seen in CPVs. The alternative idea is that charged dust could provide most of the opacity (Sanderson et al. 2023). For TIC 141146667, Figures 2 and 3 show that the transits of the Hα emitting material only partially overlap the complex photometric modulation. This implies that some of the complex photometric dips must involve additional opacity sources or spatially distinct structures.

Independent of this opacity question, our observations show that corotating clumps of cool plasma exist around a CPV. While starspots do contribute smooth signals to CPV photometric variability, the existence of these clumps would not be predicted by a "starspot-only" scenario (Koen 2021). Scenarios in which the circumstellar material is made only of dust are similarly ruled out.

The circumstellar material – either pure plasma or dusty plasma – could originate either from the star or from an external source. Plausible external sources include an undetected old disk, comets, or a close-in exoplanet. This latter scenario would make CPVs extrasolar analogs of the Jupiter-Io torus (e.g. Bagenal & Sullivan 1981), although with a very different composition.

The other analog for the CPVs are the σ Ori E variables, a rare subset of B stars with radiatively-driven winds which accumulate into warped plasma tori (Townsend & Owocki 2005; Townsend 2008). These tori tend to have dense antipodal accumulations of plasma sculpted by tilted-dipole magnetic fields, and the transits of these clumps produce broadband photometric variability through bound-free scattering (Townsend & Owocki 2005) and Thomson scattering (Berry et al. 2022). For σ Ori E and almost all of its analogs, the result is simple light curves that resemble those of eclipsing binaries, and time-dynamic Hα spectra similar to those

in Figure 3. The two known exceptions, HD 37776 and HD 64740, show complex light curves resembling CPVs (Mikulášek et al. 2020; Bouma et al. 2024) and have spectropolarimetric magnetic field maps indicating strong contributions from higher-order magnetic moments (Kochukhov et al. 2011; Shultz et al. 2018). This suggests that the photometric complexity of CPVs may be related to magnetic fields with highly multipolar contributions.

4.4. *Connection to Previous Work*

Spectra of magnetically-active, rapidly rotating stars with a wide range of masses have been previously observed to exhibit sinusoidal time-varying Balmer emission (Donati et al. 2000; Townsend & Owocki 2005; Dunstone et al. 2006; Skelly et al. 2008), similar to Figure 3. No such stars were previously known to show complex light curves (Bouma et al. 2024). One interpretation for the spectroscopic variability of these stars, and that of the analogous transient absorption features (Collier Cameron & Robinson 1989; Collier Cameron & Woods 1992; Cang et al. 2020), comes from an analogy to quiescent solar prominences, cool condensations of plasma in the solar corona that can last days to weeks (Vial & Engvold 2015). In the case of the Sun, these condensations fall back to the photosphere because gravity is stronger than any magnetic tension or centrifugal force capable of sustaining them. However it has been understood at least since work by Donati et al. (2000) that these "prominence systems" can be longitudinally extended, forming a trapped ring of plasma. While the issue of why these previously known spectroscopic variables do not show complex photometric variability remains open, plausible explanations include that they are not in the required transiting geometry, or that they lack the necessary source of opacity. What we have in the case of TIC 141146667 is a system that finally exhibits both sets of phenomena.

4.5. *Future Work: Composition, Origin, Modelling*

Pressing issues include determining the composition and origin of the circumstellar material, understanding the exact role of the stellar magnetic field, and exploring the implied space weather experienced by the close-in rocky exoplanets that, statistically (Dressing & Charbonneau 2015), are likely to be present in most CPV systems.

The material's composition – either pure plasma or dusty plasma – can be clarified by time-series optical and infrared spectrophotometry. While observations of CPVs in the optical suggest a chromaticity consistent with dust (Tanimoto et al. 2020; Günther et al. 2022; Koen 2023), a gray opacity source such as electron scattering in a plasma transiting over a spotted background star might also produce chromatic features (Rackham et al. 2018). The composition and size distribution of any dust that is present could be determined by measuring the extinction curve for a sample of CPVs from 1-20 μm. Composition and size distributions similar to debris from rocky bodies seen around white dwarfs (Reach et al. 2009) would suggest an extrinsic origin channel. Compositions and sizes similar to the interstellar medium would sug-

---

[‡] http://user.astro.wisc.edu/~townsend/static.php?ref=rrm-movies#Download_Bundles last accessed 23 April 2025.

gest that dust can condense out from M dwarf winds, similar to processes that occur around more evolved stars (Marigo et al. 2008).

The role of the star's magnetic field could be better understood through new observations, and new theory. From the modeling perspective, there is a need for rigid-field magnetohydrodynamic models to go beyond previous work (Townsend & Owocki 2005; Townsend 2008; Krtička et al. 2022) and to explore what field topologies explain the observed light curve shapes. In particular, dynamo simulations of fully-convective M dwarfs have suggested that global-scale mean fields might be confined to a single hemisphere (Brown et al. 2020); such fields would yield accumulation surfaces quite different from those that have previously been explored. Observationally, spectropolarimetry has the potential to assess both the field strength and topology. An independent constraint on magnetic field topology may also come from radio observations, which have shown (Kaur et al. 2024) that CPVs emit variable radio signals, including persistent and polarized components. Detecting radio emission produced by an electron cyclotron maser instability (e.g. Callingham et al. 2021) in particular would provide a measurement of the field strength at the site of the emitting region, which could help clarify the magnetosphere's structure.

It is currently unclear what, if any, relationship CPVs have to the close-in rocky exoplanets that exist around most M dwarfs (Dressing & Charbonneau 2015). However, a few percent of young M dwarfs show the CPV phenomenon (Rebull et al. 2020), and our data show that some of the complex photometric features occur when clumps of circumstellar material transit the star. The suggested geometric correction implies that an appreciable minority ($\gtrsim$10%) of young M dwarfs – the rapidly rotating ones with centrifugal magnetospheres – host circumstellar environments similar to the CPVs. Future studies that combine spectroscopic, polarimetric, and multi-wavelength observations, along with magnetohydrodynamic modeling, will be key to understanding the complex environments of these young stars.

APPENDIX

A. STELLAR PARAMETERS

Radial Velocity—We measured the radial velocities of TIC 141146667 from our HIRES spectra using a pipeline that we developed for rapidly rotating stars. Our method is based on template-matching against synthetic spectra produced by the PHOENIX stellar atmosphere code (Husser et al. 2013). We used the PHOENIX models with solar metallicity and alpha element abundances, and calibrated our pipeline using the standard stars described by Chubak et al. (2012). We used velocity standards spanning spectral types from G2 to M4 (Barnard's Star), irrespective of rotation rate. We used `barycorrpy` (Kanodia & Wright 2018) to calculate the velocity corrections due to Earth's motion around the solar system barycenter and due to Earth's daily rotation about its axis. Our analysis code reproduces the systemic velocities of known velocity standards (Chubak et al. 2012) with an RMS of $0.66\,\mathrm{km\,s^{-1}}$.

For TIC 141146667, we measured the radial velocities using regions near the K I (7700 Å) resonance line and three TiO bandheads (5160 Å, 5450 Å, and 5600 Å). We selected these regions because they provided the best matches between the synthetic and observed spectra. We then averaged the resulting redshift measurements over each order to produce the final measurement. We used the scatter of resulting velocity measurements between orders to assign the RV uncertainty at each epoch. The uncertainty-weighted mean systemic velocity over all epochs on 17 February 2024 was γ=0.6$\pm$1.5 km s^{-1}. The relative radial velocities about this mean are given in Table 3.

Viewing Orientation—We fitted the rotational broadening of the K I (7700 Å) resonance line using the kernel suggested by Gray (2008); taking the mean and standard deviation of the resulting value over all epochs yielded $v_{\mathrm{eq}}\sin i$=138$\pm$8 km s^{-1}, consistent with the visual line broadening $\Delta\lambda\approx$3 Å. The star's equatorial velocity v_{eq} based on its apparent size and rotation period is

Figure 4. **Spectral energy distribution** of broadband photometric magnitudes (filled markers) plotted over the best-fit BT-Settl stellar atmosphere model (Allard et al. 2012) and the associated photometric predictions (empty markers). This plot was made from an adaptation of `astroARIADNE` (Vines & Jenkins 2022). The photometry extends from the Gaia DR3 blue passband to WISE W3; the W4 passband (22 μm) did not yield a confident detection. This fit yields the star's temperature and size. The lack of excess infrared flux relative to the photospheric model sets an upper limit on emission from circumstellar dust.

130$\pm$4 km s^{-1}. While this suggests that the viewing orientation could be nearly edge-on, the formal constraint is rather weak, with $i>63°$ at 2σ (2.5$^{\text{th}}$ percentile of the inclination posterior).

No Evidence For Binarity—Any periodicity in the radial velocity time-series is ruled out at the rotation period for semi-amplitudes above 2.85 km s^{-1} (at 3σ confidence). This sets an upper limit on the mass of any putative companion at the four hour period of $m\sin i<2.4\,M_{\text{Jup}}$. Regarding possible companions at wider separations, the Gaia DR3 renormalized unit weight error (RUWE), a proxy for the goodness of fit for a single-source astrometric model to the Gaia astrometry, is 1.23, within the usual range for apparently single sources. There are no resolved companions in the Gaia DR3 point source catalog. Finally, we checked the TESS light curve for evidence of secondary photometric periods by subtracting the mean CPV signal over each sector and performing a phase-dispersion minimization analysis (Stellingwerf 1978; Bhatti et al. 2021). There were no secondary periods in the TESS data. Previous work (Bouma et al. 2024) has shown that about 30% of CPVs show evidence for excess noise above the Gaia single-source astrometric model, and about 40% of CPVs show evidence for unresolved binary companions based on the presence of secondary photometric periods. This agrees with analyses showing that multi-periodic low-mass stars are generally unresolved binaries (Tokovinin & Briceño 2018). Overall, the CPV binary fraction seems consistent with that for field M dwarfs (Winters et al. 2019), pointing to a weak or non-existent connection between the CPV phenomenon and (wide) binarity. For TIC 141146667 specifically, although we find no evidence for stellar multiplicity, our data are minimally constraining for the scenario of a low-luminosity companion ($F_1/F_2\lesssim0.1$) with apparent separation below 0.″1.

Effective temperature, radius, mass, and spectral classification—We adopted the star's effective temperature and radius measured using the spectral energy distribution (SED) fitting procedure described by (Bouma et al. 2024). To summarize, this approach used `astroARIADNE` (Vines & Jenkins 2022) with the BT-Settl stellar atmosphere models (Allard et al. 2012), assuming the (Asplund et al. 2009) solar abundances and the (Barber et al. 2006) water line lists. This approach fitted for the stellar effective temperature, radius, reddening, surface gravity, metallicity, and distance by comparing the measured broadband magnitudes against pre-computed model grids. Specifically, we performed the fit using the broadband magnitudes from Gaia DR2, APASS, 2MASS, SDSS, and WISE $W1$ and $W2$. The resulting best-fit SED is shown in Figure 4. This method has the most constraining power for the star's effective temperature (2972 ± 40 K) and radius ($0.42 \pm 0.02\,R_\odot$); the surface gravity, metallicity, and reddening are only weakly constrained. We determined the star's spectral type to be M5.5Ve by visually comparing the HIRES spectra against the photometric standards tabulated by (Bochanski et al. 2007). This result agrees with the effective temperature found from the SED fitting (Pecaut & Mamajek 2013). We measured the equivalent width of the Hα line by fitting a range of models to the time-averaged line profile shown in Figure 3, selecting the model that minimized the Bayesian information criterion, and numerically integrating this best fit model. We found a sum of two Gaussians to be the preferred model; our quoted result, EW$_{\text{H}\alpha}$=7.2$\pm$0.2 Å, comes from numerically integrating within $|\Delta v/v_{\text{eq}}| < 1$. Integrating over the entire line
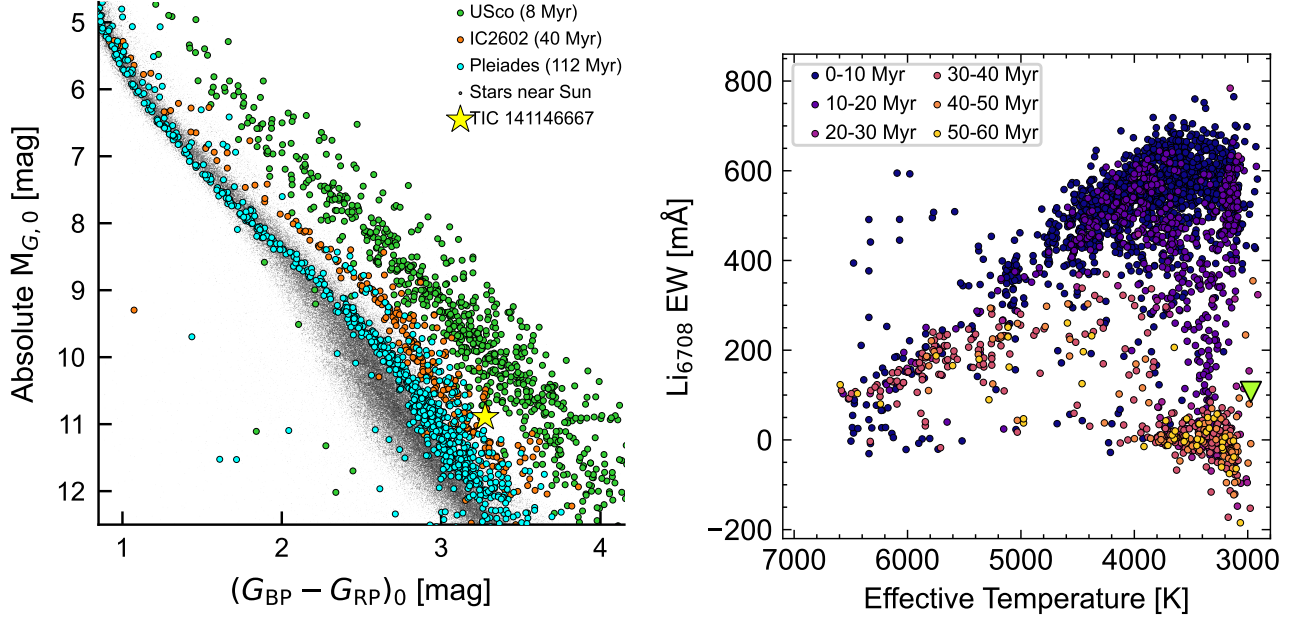
Figure 5. TIC 141146667 age diagnostics. *Left:* Dereddened Gaia DR3 color vs. absolute magnitude diagram of TIC 141146667 and comparison samples. TIC 141146667 is on the pre-main sequence; stars with the same color on the main sequence are ≈1.5 magnitudes fainter. The star's location in this diagram suggests an age of 30-150 Myr. *Right:* An upper limit on photospheric lithium for TIC 141146667 (green triangle) yields a lower bound on the star's age of ≳20 Myr. Comparison stars are from the Gaia-ESO survey (Jeffries et al. 2023); rich clusters in each age bin include NGC 2264 (4.5 Myr), λ Ori (8.7 Myr), $γ^2$ Vel (16.4 Myr), NGC 2547 (35.0 Myr), IC 2602 and IC 2391 (42.0 Myr), and NGC 2451A (50.0 Myr).

profile, including the broad wings, would yield $EW_{H\alpha}$=10.2±0.3 Å. Either value would classify the star as a weak-lined T Tauri (Briceño et al. 2019).

Given the effective temperature, stellar radius, and age range (35-150 Myr) derived below, we then estimated the stellar mass by interpolating against the PARSEC v1.2S isochrones (Chen et al. 2014). Specifically, we used the distance metric defined in Equation 8 of Bouma et al. (2024) to select the model mass closest to a given observed temperature, radius, and age. This exercise yielded a mass of $M_\star$=0.20 ± 0.01 $M_\odot$ assuming an age of 35 Myr, or a mass of 0.25 ± 0.01 $M_\odot$ assuming an age of 150 Myr. These masses imply Keplerian corotation radii $R_{cr}/R_\star$=1.75±0.07 and $R_{cr}/R_\star$=1.89±0.07, respectively; this size scale is relevant because it is theoretically expected to set the inner boundary at which corotating material might accumulate (e.g. (Townsend & Owocki 2005; Daley-Yates & Jardine 2024)). Our final quoted $M_\star$ and R_{cr} values adopt the average of these extremes and a quadrature sum of their statistical uncertainties; we caution however that a more precise age would be needed to resolve the systematic uncertainties in these parameters.

Age: No Obvious Association Membership—In Bouma et al. (2024) we previously found that over 90% of CPVs within 100 pc are associated with known young moving groups based on their positions and kinematics. TIC 141146667 is in the minority. We calculated the probability of TIC 141146667 being part of any nearby known group using BANYAN Σ v1.2 (Gagné et al. 2018). That particular model classifies it as a field star at >99.9% confidence. We also searched the local vicinity of TIC 141146667 for neighbors with similar projected on-sky velocities using `comove` (Tofflemire et al. 2021). This yielded no strong candidates for co-moving stars with projected tangential velocities Δv_T<5 km s^{-1} that share its isochronal youth.

Age: Isochrones—The color and absolute magnitude of TIC 141146667 suggest that it is a pre-main sequence M dwarf, similar to all other known CPVs (Stauffer et al. 2017, 2021; Bouma et al. 2024). The star's proximity (d=58 pc) and high galactic latitude (b=+53°) yield negligible interstellar reddening along the line of sight (Green et al. 2019). Figure 5 shows the location of TIC 141146667 in the color–absolute magnitude diagram (CAMD) relative to young stellar populations including Upper Scorpius (USco), IC 2602, and the Pleiades. To make this diagram, we adopted the USco members in the δ Sco and σ Sco sub-associations from Ratzenböck et al. (2023), and the IC 2602 and Pleiades members from Hunt & Reffert (2024). We assumed an average V-band extinction A_V={0.12, 0.11, 0.10} mag for USco (Pecaut & Mamajek 2016), IC 2602 (Hunt & Reffert 2024), and the Pleiades (Hunt & Reffert 2024) respectively, and ages of 8 Myr (Ratzenböck et al. 2023), 40 Myr (Randich et al. 2018), and 112 Myr (Dahm 2015) for each respective cluster. We dereddened the photometry using the extinction coefficients $k_X \equiv A_X/A_0$ tabulated in (Gaia Collaboration et al. 2018), assuming that $A_0 = 3.1E(B-V)$.

Figure 5 shows that TIC 141146667 falls between the USco and Pleiades sequences, and approximately overlaps IC 2602. However, the precision of the implied age is set by the intrinsic scatter of these calibration sequences; the most luminous stars in the Pleiades of the same color have a similar absolute magnitude as TIC 141146667. Previous work by Stauffer et al. (2021) has also noted that in the Gaia passbands, CPVs tend to be photometrically redder and more luminous than single stars in any given cluster, similar to other rapid rotators. While this effect complicates any attempt at age inference based on the Gaia photometry, it suggests that the Pleiades may be a better comparison population than IC 2602. We take the star's location in the color–absolute magnitude diagram to suggest age bounds $t_{CAMD} \sim 30\text{-}150$ Myr.

Age: Lithium—The depletion of lithium due to ^{7}Li(p, α)^{4}He burning in the cores of low-mass stars has been studied for over sixty years (Hayashi & Nakano 1963; Bildsten et al. 1997; Burke et al. 2004). Wood et al. (2023) provided a recent overview: an abbreviated summary is that sufficiently cool and young M dwarfs show the 6707.8 Å doublet in absorption, $\gtrsim 10\%$ below their continua. However unlike for Sun-like stars, the continuum for M dwarfs is challenging to define due to their molecular absorption. We therefore attempted a lithium measurement by constructing a wavelength-binned and Doppler-corrected TIC 141146667 spectrum, assigning its uncertainties based on the measured scatter across the five hour dataset. We then compared this average spectrum against the nearest matching M6 template from Bochanski et al. (2007). The data show a small depression near the expected lithium wavelength, potentially consistent with the $\Delta\lambda \approx 3$ Å line broadening. This feature nominally yields $EW_{Li} = 71^{+18}_{-13}$ mÅ, where the statistical uncertainties are evaluated using a bootstrap resampling technique from the statistical uncertainties in the HIRES spectrum. However, the systematic uncertainties associated with the continuum normalization are likely comparable to the amplitude of this feature; we therefore treat the result of this measurement as a 2σ upper limit: $EW_{Li} < 107$ mÅ.

Despite ambiguity in the details, what can be stated with confidence is that lithium is not abundant in the spectrum of TIC 141146667. Figure 5 compares our upper limit against the equivalent width measurements reported by Jeffries et al. (2023) based on the Gaia-ESO spectroscopic survey; Figure 8 shows the associated raw spectra. If the star were $\lesssim 20$ Myr old, at its temperature we would expect to see lithium in abundance (> 400 mÅ). Since we do not, we can set an empirical bound on the lithium-derived age of $t_{Li,emp} \gtrsim 20$ Myr. The Feiden (2016) lithium isochrones provide a point for theoretical comparison, and suggest that since $M_K \approx 6.67$ mag, $t_{Li,th} \gtrsim 35$ Myr is the theoretical age at which complete depletion occurs in a star with this luminosity (see e.g. Figure 7 from Wood et al. 2023).

Age: Summary—The main indicators for the youth of TIC 141146667 are *i)* that it is a complex periodic variable, and *ii)* that it is 1.5 magnitudes brighter (four times more luminous) than main sequence stars of the same color, while showing no indicators for binarity. Being a CPV suggests that the star is young because a previous CPV search unbiased in age found 90% of its detections to be in $\lesssim 200$ Myr old clusters (Bouma et al. 2024); the remaining 10% were not associated with any coeval population. Similarly, studies of rotation in $\lesssim 100$ Myr clusters serendipitously found $\approx 50\text{-}100$ examples of the class (Rebull et al. 2016; Stauffer et al. 2017, 2018; Rebull et al. 2018; Zhan et al. 2019; Rebull et al. 2020; Stauffer et al. 2021; Rebull et al. 2022; Popinchalk et al. 2023), whereas analogous studies of Praesepe and the Hyades did not report any evidence for CPVs in a set of approximately one thousand ≈ 700 Myr stars (Rebull et al. 2017; Douglas et al. 2019; Rampalli et al. 2021). Regarding the isochronal age constraint, the Pleiades (112 Myr, Dahm 2015) shows a few stars of equal luminosity and the same temperature, suggesting a photometric isochronal age upper limit $\lesssim 150$ Myr. The weak lithium absorption suggests an age of at least 20 Myr based on an empirical comparison using Gaia-ESO spectra, or at least 35 Myr based on the Feiden (2016) isochrones. These considerations yield our adopted age range of 35-150 Myr.

B. DETAILED BEHAVIOR OF Hα: MODEL AND IMPLICATIONS

A model for the time-dynamic Hα spectrum—While Figure 3 shows that clumps of circumstellar material exist around TIC 141146667, there is value in quantifying the exact orbital periods, velocities, and velocity dispersions of these clumps. These quantities can constrain the physical dimensions of the emitting region, and can also clarify whether the spectroscopic period agrees with the photometric period.

Given that a full radiative transfer simulation was outside our scope, we opted to construct a phenomenological model aimed at capturing the emission from the circumstellar material. We did this by fitting each spectral epoch with a multi-component gaussian, after having subtracted the time-average line profile as in Figure 3e. The results of this exercise are shown in Figure 6; details in the implementation and interpretation follow.

To implement this model, we assumed that the "inner" ($K_{inner} \approx 2.5\, v_{eq}$) clump would be well-fit by a sum of two gaussians because it is visually double-peaked in the raw data from $\phi = 0.15\text{-}0.35$ and $\phi = 0.65\text{-}0.85$ (Figure 3b). We assumed that the "outer" ($K_{outer} \approx 3.9\, v_{eq}$) clump would be better fit by a single gaussian, based on its behavior from $\phi = 0.6\text{-}0.9$. Each gaussian component has three free parameters at each spectral epoch: the mean μ, standard deviation σ, and amplitude A. We labelled the inner component's two gaussians $i = \{0, 1\}$, and the single outer component as $i = 2$. Given the complexity of the line profile data (Figure 6 left column), the likelihood function for this model is multimodal. We therefore imposed the prior constraints that $A_i \sim \mathcal{U}[0, 1]$, $\sigma_i / v_{eq} \sim \mathcal{U}[0, 1]$, and further assumed $\mu_i(t) \sim \mathcal{U}[K_{inner}\sin(\phi(t)) - v_{eq}, K_{inner}\sin(\phi(t)) + v_{eq}]$ for the inner two components, and $\mu_2(t) \sim \mathcal{U}[K_{outer}\sin(\phi(t)+\pi) - 2v_{eq}, K_{outer}\sin(\phi(t)+\pi) + 2v_{eq}]$ for the outer component. This prior on the means mitigates multimodality in the likelihood by requiring the mean velocity of each component to be within a one or two v_{eq} of the time-variable sinusoid suggested by visual inspection. We fitted each component to the data *independently* using scipy's non-

Figure 6. Time-variable fit to Hα line profiles. *Left column:* Raw spectrum at each epoch f_λ minus the time-averaged spectrum $f_{\langle t \rangle}$ (as in Figure 3e). Underplotted sinusoids are not fits; they are meant to guide the eye. *Middle columns:* Model of emission from the inner clump (sum of two gaussians) and the outer clump (single gaussian), plotted over the data. *Right column:* Residual of the left column after subtracting the sum of the two middle columns, leaving variability in the line core. Appendix B discusses the use of this model.

576 linear least squares `curve_fit` implementation (Virtanen et al. 2020), and scaled the resulting parameter covariance matrix by
577 a constant factor to match the sample variance of the residuals. The resulting means, amplitudes, and standard deviations for each
578 component are given in Table 4.
579   Caution is required in interpreting this model's results. At some epochs there are no significant spectral features around any
580 component's prior. During such epochs, e.g. the "outer" clump at ϕ=1.07, the model fits noise, not signal. At other times, the
581 model underfits. For instance, the sudden blue rise near ϕ=0.2 is poorly described by a gaussian; the assumed functional form
582 is one of convenience. Finally, the model fits the $i = \{0, 1\}$, and $i = 2$ components independently. At ϕ=0.0 and 1.0, Figure 6

Figure 7. a, Orbits fit to mean radial velocities (RVs) extracted from Hα profile fits in Figure 6. Radial velocities on the vertical axis are in units of the equatorial velocity, v_{eq}=130 km s⁻¹. Each marker denotes the best-fit gaussian mean at a given epoch. Solid circles were adopted in the fits; transparent X markers were excluded due to reliability concerns (see text). The inner double-peaked clump is shown in violet and orange; the outer clump is shown in green. Five model draws from each posterior probability distribution are plotted. **b,** Idealized emissivity from mean model fits in Panel a, assuming a constant emission amplitude and velocity width σ=0.25 v_{eq} and neglecting eclipses.

suggests that the emission might come from either the inner or outer components. Physically however, at this epoch the inner clump is in transit, and the outer clump is passing behind the star. At ϕ=0.0, the double-peaked emission profile also matches that seen shortly afterward (at ϕ=0.14) when the inner clump is viewed off-disk. A physical interpretation of the model would therefore discard the outer clump results at this particular epoch, because its emission would be blocked by the star.

Accounting for these caveats, we used the results from Table 4 to quantify the orbital periods and velocity semi-amplitudes of the clumps. Figure 7a shows the results assuming circular orbits; considering the Bayesian information criterion, we found no reason to prefer eccentric orbits. By visually inspecting Figure 6, we excluded epochs where our gaussian profile fitting failed to either detect or else adequately represent the circumstellar emission. We then used NumPyro to sample the Gaussian likelihood for a Keplerian orbit with the NUTS algorithm (Phan et al. 2019). We used the measurement uncertainties from each estimated mean radial velocity value and included an additional jitter term in quadrature. This procedure yielded orbital periods and semi-amplitudes of P_0=3.92 ± 0.03 hr, K_0/v_{eq}=2.07±0.04; P_1=3.92 ± 0.06 hr, K_1/v_{eq}=2.88±0.10; and P_2=3.88 ± 0.20 hr, K_1/v_{eq}=3.88±0.25. The periods for the inner double-peaked clump are therefore consistent with the photometric 3.930±0.001 hr period within a precision of two minutes. The "period" for the outer clump is ambiguous because the Hα data only support the idea of a periodic orbit of material well-fit by gaussian emission from ϕ≈0.5-1.0. From ϕ=0-0.2, there is no detectable emission, and from ϕ=0.2-0.4, the emission spans 1-4 v_{eq} without taking a clear gaussian shape. While the outer-most edge of this ϕ=0.2-0.4 emission provides a plausible match to the expectation of a circular orbit, the idea of invoking a particular functional form for this component seems fine-tuned. We instead emphasize that although this emission is present, its variability in time is inconsistent with the idea of a stable clump of material. Additional observations would be needed to conclusively determine whether or not this component of the system is long-lived.

For Figure 7b, we then used the mean orbits from Figure 7a to generate sinusoidal-in-time gaussians, similar to the observations. We assumed a constant emission amplitude and velocity width σ=0.25 v_{eq} for this exercise, and normalized each gaussian to unit amplitude; the colorbar in Figure 7b thus masks the non-physical additive contribution near the zero-crossing of velocity. Compared to the behavior of the data at ϕ=0.2-0.5 (Figure 3), this is highly idealized. Nonetheless, this exercise indicates that the transit of the inner clump lasts ≈22% of each cycle, with a slight asymmetry around ϕ=0.

Physical dimensions of the emitting region—The measured velocity widths from the circumstellar emission contain information about the size of the emitting region via the condition for rigid corotation. Consider a clump in cylindrical coordinates with arbitrary radial extent r, azimuthal extent ℓ, and height z. A range of shapes, including an "arc" with $\ell \gg r$, a "spoke" with $r \gg \ell$, and a "blob" with $r \approx \ell \approx z$ are all a priori possible. However, at quadrature, the observed velocity width of emission is sensitive to the radial extent of the circumstellar material. At mid-transit, the observed velocity width is sensitive to the azimuthal extent. An arc configuration would minimize the observed velocity width σ at quadrature, and maximize it during transit, with
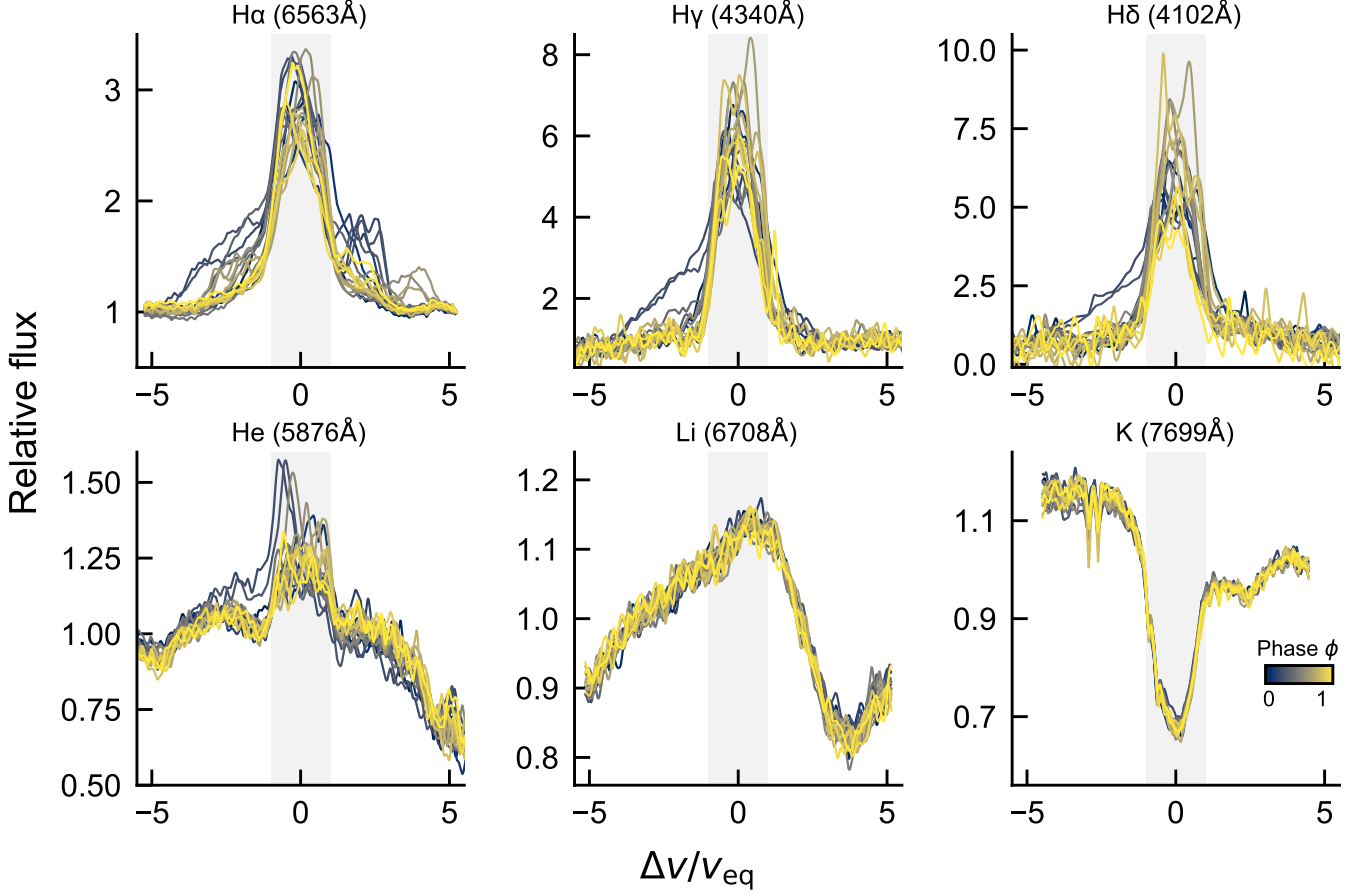
Figure 8. Time evolution of the Keck/HIRES spectra from 17 February 2024. We made this plot by applying a windowed outlier rejection to remove cosmic rays and then smoothing each spectrum with a Gaussian filter. The horizontal axis shows the velocity relative to each line's rest wavelength, normalized by the stellar equatorial velocity. Hα is the only Balmer line to show periodic variability similar to Figure 3. The He 5876 Å line shows a time-dynamic blueshift. Li 6708 Å shows no obvious absorption.

$\gtrsim 100\,\mathrm{km\,s^{-1}}$ variations in between. This is not observed. The arc geometry, and by a similar argument the spoke geometry, can thus be discarded.

At quadrature, the inner clumps show $\sigma_i \approx 0.24\,v_{\mathrm{eq}}$, implying that 68% of the emission comes from a volume with length in the radial dimension $r_i = 2\sigma_i/\Omega = 0.48\,R_\star$, and that 95% of the emission comes from within $0.96\,R_\star$. These values have relative uncertainties of $\approx 5\%$, based on the uncertainties in the measured velocity dispersions. The two inner clumps are centered at orbital distances of $2.07\,R_\star$ and $2.88\,R_\star$. There is therefore physical overlap in their spatial distributions. These two clumps could in fact be a single clump with an optically thick Hα line core. Regardless of this nuance, the implication is that the full length in the radial dimension of these two inner emitting clumps is approximately equal to the star's diameter. At mid-transit, these inner clumps have a similar velocity dispersion, although with greater uncertainty due to the differences between the ϕ=0 and ϕ=1 transits (see Figure 6). This suggests a 1σ emission contour in the azimuthal dimension with a length of $\ell \approx 0.5\,R_\star$.

The vertical height of the emitting region is less constrained because the system is consistent with being viewed edge-on. However, one constraint does come if one assumes that the TESS transit depth scales with the projected Hα emission area ℓz. More specifically, one can evaluate an "effective area" blocked by a two-dimensional gaussian blob passing over a star by integrating the local gaussian weight over the stellar surface. For instance, if $\ell \approx z \approx 0.24\,R_\star$, then $\iint \exp\left(-\left(x^2/2\sigma_x^2 + y^2/2\sigma_y^2\right)\right)\,\mathrm{d}x\,\mathrm{d}y$ suggests 11.5% of the star being "blocked", a geometric factor which would need to be in turn multiplied by an unknown opacity factor to produce the observed transit depth ($\delta \approx 5\%$). In general though, there is a degeneracy between z and this opacity factor; larger vertical heights are allowed for lower optical depths in absorption, and vice-versa. This constraint also implicitly assumes that the optically thick material is well-mixed with the hydrogen, which may not be accurate.

C. SPECTROSCOPIC VARIABILITY

Figure 8 shows a few regions of interest in the HIRES spectra, which cover 3650-7960 Å. Hβ falls in an inter-order gap and was not observed. Higher order Balmer lines including Hγ and Hδ ($n = 5 \rightarrow 2$ and $n = 6 \rightarrow 2$) do show variability outside the line core. However, this variability is not clearly periodic in the same manner as the emission seen in Hα. This could be because there are insufficient hydrogen ions in the relevant excited states, or because the spectra have lower precision in these bluer regions. The Ca HK doublet is also detected in emission, while the continuum near it is not. Chromospheric emission from the magnesium triplet is also detected, but these lines are too blended to be usable.

Figure 8 provides a novel view on the blue excess that appeared at $\phi \approx 0.2$ in Hα, Hγ, Hδ, and He 5876 Å. At the same epoch, Hα additionally shows a red clump of emission, and Hγ and Hδ are also broadened on the red wing. The rise of this emission in <15 minutes might suggest a more sudden flow, rather than a stable, periodic component. For instance, a stellar flare might be connected to such a sudden rise. However, this idea seems incompatible with the sinusoidal emission seen from $\phi \approx 0.3$-1.0, and with the fact that flares typically excite iron lines in the blue HIRES orders, which are not observed. More time-series spectroscopy would be needed to clarify this type of variability, in particular whether it is periodic or stochastic. The gap in the TESS photometry (Figure 2) additionally clouds the interpretability of this event.

Finally, the Li I 6708 Å doublet, which shows no obvious absorption, as well as the broad K I 7699 Å resonance line are both visible in Figure 8. In the latter, narrow telluric absorption features overlap the blue wing of the line. Neither of these regions shows any notable variability.

D. PROPERTIES OF THE PLASMA AND MAGNETOSPHERIC ENVIRONMENT

The physical conditions inside the plasma clumps, in particular the hydrogen number density, plasma temperature, ionization fraction, and magnetic field strength can be estimated from the available data. We caution that the following estimates are order of magnitude calculations that assume a simple uniform-density plasma: detailed considerations of radiative transfer are a worthy topic for future work, but are beyond the scope of this article.

Circumstellar Hα emission might be sourced either from resonant scattering of stellar Hα photons, or from radiative recombination. We neglect scattering because Figure 3 and Figure 8 show the amplitude of the circumstellar Hα emission varying by a factor of ≈ 5, in a manner uncorrelated with any variability in the chromospheric line core. The volume emissivity under case B recombination can be written

$$j_{H\alpha} = n_e n_p \alpha_{H\alpha}^{\text{eff}} h\nu_{H\alpha}, \tag{D1}$$

where n_e and n_p are the electron and proton densities, and $\alpha_{H\alpha}^{\text{eff}}$ is the effective recombination coefficient, defined to include all recombination routes that produce an Hα photon. For hydrogen with temperatures between 1,000-10,000 K, $\alpha_{H\alpha}^{\text{eff}}$ is typically on the order of 10^{-12} to 10^{-13} cm^3 s^{-1} (Hummer & Storey 1987; Draine 2011). Neglecting the effects of atoms other than hydrogen, we can assume an ionization fraction x, such that $n_e = n_p = x n_H$, for n_H the hydrogen number density. Let $L_{H\alpha} = j_{H\alpha} V$, for V the volume of the emitting hydrogen. The luminosity of circumstellar hydrogen emission, $L_{H\alpha}$, is an observable: our SED fitting routine yields $L_\star \approx 0.012\,L_\odot$, which implies that the stellar Hα line radiates at $\approx 1.0 \times 10^{28}$ erg s^{-1}. The luminosity of the clumps $L_{H\alpha}$ are of order one tenth that of the star. If we approximate the emitting volume as a homogeneous sphere of radius r, we can write

$$n_H = 1 \cdot 10^{11}\,\text{cm}^{-3} \left(\frac{0.5}{x}\right) \left(\frac{L_{H\alpha}}{10^{27}\,\text{erg s}^{-1}} \frac{10^{-13}\,\text{cm}^3\,\text{s}^{-1}}{\alpha_{H\alpha}^{\text{eff}}}\right)^{1/2} \left(\frac{0.1\,R_\odot}{r}\right)^{3/2}. \tag{D2}$$

For a uniform density clump, this suggests a total gas mass of $M_{\text{gas}} \approx 2 \times 10^{17}$ g. We emphasize that Equation D2 in intended to provide only an order of magnitude estimate for the number density implied by the observed Hα emission. In detail, the effective recombination rate and the ionization fraction each vary with density and temperature; a more thorough estimate would iteratively solve the equations of detailed balance and radiative transfer (e.g. Collier Cameron & Robinson 1989 Figure 8), and potentially also consider departures from local thermodynamic equilibrium.

Finally, a constraint on the magnetic field strength at the site of the clump follows from the requirement that the magnetic pressure exceed the thermal pressure, $B_c^2/8\pi > n_H kT$. Although we do not know the plasma temperature, if it were significantly beyond 1,000-10,000 K, we would either fully ionize the hydrogen, or not ionize enough of it. The field strength at the clump must therefore exceed

$$B_c \gtrsim 1\,\text{G} \left(\frac{n_H}{1 \times 10^{11}\,\text{cm}^{-3}} \frac{T}{3000\,\text{K}}\right)^{1/2}. \tag{D3}$$

Given that the average surface magnetic field strengths of low-mass stars have been measured to span hundreds to thousands of Gauss (Donati & Landstreet 2009; Kochukhov 2021; Reiners et al. 2022), this bound is easily met at orbital distances of 2-4 $R_\star$.

E. UPPER AND LOWER BOUNDS ON DUST

The material's composition – either pure plasma, or a dusty plasma – is not known. The idea of dust being present seems plausible given observations of chromatic transits in analogous objects (Tanimoto et al. 2020; Günther et al. 2022; Koen 2023). However, this scenario is highly constrained. An upper limit on the amount of hot dust follows from the lack of an infrared excess. A lower limit follows if one assumes that most of the broadband optical depth comes from dust absorption and scattering, rather than any radiative processes associated with the plasma.

Regarding the upper limit, Figure 4 shows the SED. While AllWISE (Cutri et al. 2021) yielded a confident W3 detection (9.8σ) consistent with the photospheric extrapolation from bluer bandpasses, the W4 extraction yielded only a marginal indication (1.7σ) of detectable flux. Similar to other CPVs (Stauffer et al. 2017; Bouma et al. 2024), the photometric uncertainties from WISE W1 and W2 allow at most a $\lesssim2\%$ excess at 3-5 μm relative to the stellar photosphere, and a $\lesssim5\%$ excess at 10 μm (W3). To estimate the implied mass bound, we assume a dust temperature T_d=1500 K, typical for dust near the star (see Zhan et al. 2019 for discussion regarding dust sublimation). We then treat emission from the dust and star as Planck functions, and require $L_d < fL_\star$, where the factor f is set by the photometric precision of WISE and L_d is the bolometric dust luminosity. Given the reported uncertainties, we numerically find $f < 6\cdot10^{-3}$. From the Stefan-Boltzmann law we can then write $A_d < f(T_\star/T_d)^4 Q_{em}^{-1}(4\pi R_\star)^2$, for A_d the total emitting surface area of the dust, and Q_{em} an emission efficiency parameter. Converting this constraint to a dust mass requires an assumption regarding the grain properties. We assume a grain density ρ_d=3 g cm^{-3} typical for silicate grains, a fixed grain size a=1 μm, and no self-absorption. This enables the assumption that $A_d = N\pi a^2$, for N the total number of dust grains. This in turn yields an upper limit on the dust mass of

$$M_{dust} \lesssim 4\cdot10^{17}\,\text{g} \left(\frac{f}{6\cdot10^{-3}}\right) \left(\frac{T_\star}{3000\,\text{K}}\frac{1500\,\text{K}}{T_d}\right)^4 \left(\frac{Q_{em}}{1}\right)^{-1} \left(\frac{R_\star}{0.4\,R_\odot}\right)^2 \left(\frac{a}{1\,\mu\text{m}}\right) \left(\frac{\rho_d}{3\,\text{g\,cm}^{-3}}\right). \tag{E4}$$

The analogous lower limit follows from requiring the optical depth from absorption and scattering τ to be at least unity. The optical depth can be written $\tau = n\sigma\ell$, where σ is the cross-section, n is the number density, ℓ is the path length. For spherical dust grains in the optical, $\sigma = Q_{ext}\pi a^2$, where Q_{ext} is the extinction efficiency parameter, tabulated e.g. by Croll et al. (2014) in their Figure 13. Sanderson et al. (2023) calculated the relevant cloud mass for this problem assuming a spherical dust clump of size r, and they found

$$M_{dust} \gtrsim 2\cdot10^{15}\,\text{g} \left(\frac{\tau}{1}\right) \left(\frac{Q_{ext}}{3}\right)^{-1} \left(\frac{r}{0.1\,R_\star}\frac{R_\star}{0.4\,R_\odot}\right)^2 \left(\frac{a}{1\,\mu\text{m}}\right) \left(\frac{\rho_d}{3\,\text{g\,cm}^{-3}}\right). \tag{E5}$$

Three relevant objects for comparison include solar prominences, planetesimals, and comets. Prominences of the Sun have gas masses of 10^{14} g-10^{16} g (Vial & Engvold 2015). A planetesimal of mass $\approx10^{15}$ g with a bulk density of 1 g cm^{-3} would have a diameter of order one kilometer. Halley's comet has a mass of order 10^{17} g (Rickman 1989), of which $\sim10^{14}$ g is shed per orbit, most of which inspirals toward the Sun due to Poynting-Robertson drag.

To summarize, if dust is responsible for the broadband variability of CPVs, it would need to be concentrated in clumps with masses in the range of 10^{15}-10^{17} g. Given $M_{gas}\approx2\times10^{17}$ g from Appendix D, the allowed dust masses imply M_{gas}/M_{dust} ranges of 1-100. More careful measurements of this ratio—in particular by inferring the dust mass through high precision infrared spectrophotometry—could provide a path for distinguishing the scenario of a trapped stellar outflow from an accumulation of externally-sourced material. While there are several plausible external sources, feeding through a low-mass disk in particular cannot be ruled out based on typical disk depletion times (Haisch et al. 2001). Observations of infrared excesses and accretion signatures in low-mass stars tens of millions of years old suggest a broad lifetime distribution for such disks (Silverberg et al. 2020; Lee et al. 2020; Gaidos et al. 2022; Pfalzner & Dincer 2024).

Parameter	Host	Source
	Identifiers	
TIC	141146667	TESS
Gaia	860453786736413568	Gaia DR3
	Astrometry & Radial Velocity	
α_{2000}	11:05:15.09	Gaia DR3
δ_{2000}	+59 15 05.57	Gaia DR3
μ_α (mas yr^{-1})	-73.933 ± 0.022	Gaia DR3
μ_δ (mas yr^{-1})	32.262 ± 0.024	Gaia DR3
π (mas)	17.324 ± 0.025	Gaia DR3
RUWE	1.23	Gaia DR3
RV (km s^{-1})	0.61 ± 1.47	HIRES
	Photometry	
$TESS$ (mag)	13.283 ± 0.010	TIC8
G (mag)	14.701 ± 0.002	Gaia DR3
G_{BP} (mag)	16.664 ± 0.008	Gaia DR3
G_{RP} (mag)	13.398 ± 0.006	Gaia DR3
G_{BP}-G_{RP} (mag)	3.276 ± 0.010	Gaia DR3
J (mag)	11.401 ± 0.022	2MASS
H (mag)	10.793 ± 0.021	2MASS
K_s (mag)	10.473 ± 0.016	2MASS
$W1$ (mag)	10.276 ± 0.023	ALLWISE
$W2$ (mag)	10.070 ± 0.020	ALLWISE
$W3$ (mag)	9.838 ± 0.045	ALLWISE
	Physical Properties	
$T_{\rm eff}$ (K)	2972 ± 40	SED fit
$R_\star$ ($R_\odot$)	0.42 ± 0.02	SED fit
$L_\star$ ($L_\odot$)	0.0126 ± 0.0012	SED fit
$P_{\rm rot}$ (hours)	3.930 ± 0.001	TESS
$v_{\rm eq}$ (km s^{-1})	130±4	Derived
$v_{\rm eq}\sin i_\star$ (km s^{-1})	138 ± 8	HIRES
$i_\star(^\circ)$	>63	Derived
A_V (mag)	0	(Green et al. 2019)
$M_\star$ ($M_\odot$)	0.22 ± 0.02	PARSEC (Chen et al. 2014)
$EW_{\rm Li}$ (mÅ)	<107	HIRES (2σ)
$t_{\rm CAMD}$ (Myr)	30-150	Gaia DR3
$t_{\rm Li,emp}$ (Myr)	>20	HIRES, (Jeffries et al. 2023)
$t_{\rm Li,th}$ (Myr)	>35	HIRES, (Feiden 2016)
$t_{\rm adopted}$ (Myr)	35-150	–

Table 2. Properties of TIC 141146667. References: Gaia DR3 (Gaia Collaboration et al. 2023), TESS (Ricker et al. 2015), TIC8 (Stassun et al. 2019), 2MASS (Skrutskie et al. 2006), ALLWISE (Cutri et al. 2021).

Time [BJD$_{\text{TDB}}$]	RV (km s^{-1})	σ_{RV} (km s^{-1})
2460357.954919	2.73	5.86
2460357.965845	-4.40	2.37
2460357.976770	-0.19	2.64
2460357.987698	3.84	2.87
2460357.998619	7.53	7.53
2460358.009538	-1.98	1.44
2460358.020462	1.02	1.21
2460358.031383	0.64	7.03
2460358.042306	-2.91	2.71
2460358.053228	8.93	6.75
2460358.064154	5.95	8.84
2460358.075075	-2.25	3.06
2460358.085996	1.84	1.34
2460358.096918	2.41	8.24
2460358.107839	-7.04	3.94
2460358.118760	-2.24	3.07
2460358.129683	-2.83	7.55
2460358.140606	-0.59	2.26
2460358.151527	1.84	2.91
2460358.162448	4.54	3.95
2460358.173368	6.21	12.14

Table 3. TIC 141146667 radial velocities relative to the systemic velocity based on the 7699 Å resonance line and TiO bandheads.

BTJD	μ_0	μ_1	μ_2	σ_0	σ_1	σ_2	A_0	A_1	A_2
3357.960099	-0.725 ± 0.028	-1.416 ± 0.026	0.177 ± 0.019	0.39 ± 0.03	0.18 ± 0.03	0.59 ± 0.02	0.51 ± 0.01	0.23 ± 0.04	0.29 ± 0.01
3357.970746	-0.192 ± 0.007	0.498 ± 0.010	0.100 ± 0.014	0.23 ± 0.01	0.24 ± 0.01	0.55 ± 0.01	0.50 ± 0.01	0.37 ± 0.01	0.42 ± 0.01
3357.981672	0.895 ± 0.051	1.771 ± 0.076	-1.470 ± 0.113	0.40 ± 0.02	0.40 ± 0.10	0.09 ± 0.11	0.67 ± 0.05	0.34 ± 0.04	0.03 ± 0.03
3357.993524	1.536 ± 0.011	2.202 ± 0.015	-3.787 ± 0.049	0.25 ± 0.01	0.29 ± 0.01	0.72 ± 0.05	0.55 ± 0.01	0.46 ± 0.01	0.05 ± 0.00
3358.003594	1.974 ± 0.007	2.588 ± 0.006	-2.749 ± 0.020	0.26 ± 0.01	0.22 ± 0.00	1.00 ± 0.02	0.64 ± 0.01	0.67 ± 0.01	0.43 ± 0.01
3358.015249	2.027 ± 0.003	2.666 ± 0.003	-2.370 ± 0.015	0.24 ± 0.00	0.20 ± 0.00	1.00 ± 0.01	0.62 ± 0.00	0.60 ± 0.00	0.56 ± 0.00
3358.024971	1.790 ± 0.004	2.469 ± 0.006	-2.138 ± 0.011	0.24 ± 0.00	0.26 ± 0.00	0.77 ± 0.01	0.53 ± 0.00	0.38 ± 0.00	0.31 ± 0.00
3358.036522	0.584 ± 0.008	1.399 ± 0.009	-1.584 ± 0.009	0.18 ± 0.01	0.40 ± 0.01	0.89 ± 0.01	0.35 ± 0.01	0.39 ± 0.00	0.62 ± 0.00
3358.047668	0.328 ± 0.014	0.685 ± 0.010	-0.969 ± 0.017	0.07 ± 0.01	0.13 ± 0.01	0.46 ± 0.02	0.14 ± 0.02	0.28 ± 0.02	0.52 ± 0.02
3358.058824	-0.646 ± 0.005	-1.474 ± 0.066	0.891 ± 0.079	0.23 ± 0.00	0.25 ± 0.07	0.14 ± 0.08	0.51 ± 0.01	0.10 ± 0.01	0.09 ± 0.04
3358.069519	-0.388 ± 0.104	-1.669 ± 0.023	2.646 ± 0.020	0.40 ± 0.07	0.40 ± 0.02	0.53 ± 0.02	0.47 ± 0.04	0.33 ± 0.01	0.22 ± 0.01
3358.080468	-1.748 ± 0.009	-2.483 ± 0.010	3.526 ± 0.009	0.25 ± 0.01	0.33 ± 0.01	0.55 ± 0.01	0.28 ± 0.01	0.32 ± 0.00	0.32 ± 0.00
3358.091255	-2.119 ± 0.007	-2.868 ± 0.007	3.960 ± 0.005	0.26 ± 0.01	0.23 ± 0.01	0.40 ± 0.01	0.34 ± 0.01	0.29 ± 0.01	0.39 ± 0.00
3358.101671	-2.019 ± 0.006	-2.731 ± 0.008	3.758 ± 0.005	0.20 ± 0.01	0.24 ± 0.01	0.43 ± 0.01	0.29 ± 0.01	0.25 ± 0.01	0.23 ± 0.00
3358.112713	-1.581 ± 0.020	-2.141 ± 0.043	2.867 ± 0.019	0.19 ± 0.02	0.29 ± 0.03	0.40 ± 0.02	0.18 ± 0.02	0.13 ± 0.01	0.12 ± 0.00
3358.123928	-0.624 ± 0.006	-1.312 ± 0.076	0.824 ± 0.012	0.09 ± 0.01	0.22 ± 0.08	0.44 ± 0.01	0.18 ± 0.01	0.02 ± 0.01	0.32 ± 0.01
3358.135236	-0.012 ± 0.011	-0.208 ± 0.012	-0.192 ± 0.012	0.03 ± 0.01	0.11 ± 0.01	0.12 ± 0.01	0.12 ± 0.04	0.25 ± 0.02	0.25 ± 0.02
3358.146555	1.007 ± 0.100	1.622 ± 0.048	-1.789 ± 0.045	0.06 ± 0.11	0.31 ± 0.06	0.04 ± 0.05	0.02 ± 0.04	0.12 ± 0.02	0.05 ± 0.05
3358.156693	1.603 ± 0.018	2.444 ± 0.024	-4.408 ± 0.197	0.14 ± 0.02	0.23 ± 0.03	1.00 ± 0.17	0.14 ± 0.02	0.14 ± 0.01	0.05 ± 0.00
3358.169147	1.543 ± 0.007	2.152 ± 0.013	-3.885 ± 0.031	0.14 ± 0.01	0.39 ± 0.01	1.00 ± 0.04	0.23 ± 0.01	0.27 ± 0.00	0.10 ± 0.00
3358.177978	1.588 ± 0.037	2.828 ± 0.005	-4.378 ± 0.053	0.40 ± 0.03	0.02 ± 0.01	0.75 ± 0.06	0.33 ± 0.01	0.11 ± 0.03	0.12 ± 0.01

Table 4. Best-fit parameters from multi-gaussian model fit to Hα line profiles. Units for μ_i and σ_i are v_{eq} ($130\,\mathrm{km\,s^{-1}}$). These results should be treated with caution; only a subset of the spectral epochs yielded statistically significant detections of the circumstellar emission (see Figure 6).

REFERENCES

Allard, F., Homeier, D., & Freytag, B. 2012, Philosophical Transactions of the Royal Society A: Mathematical, Physical and Engineering Sciences, 370, 2765, doi: 10.1098/rsta.2011.0269

Asplund, M., Grevesse, N., Sauval, A. J., & Scott, P. 2009, ARA&A, 47, 481, doi: 10.1146/annurev.astro.46.060407.145222

Astropy Collaboration, Robitaille, T. P., Tollerud, E. J., et al. 2013, A&A, 558, A33, doi: 10.1051/0004-6361/201322068

Astropy Collaboration, Price-Whelan, A. M., Sipőcz, B. M., et al. 2018, AJ, 156, 123, doi: 10.3847/1538-3881/aabc4f

Astropy Collaboration, Price-Whelan, A. M., Lim, P. L., et al. 2022, ApJ, 935, 167, doi: 10.3847/1538-4357/ac7c74

Bagenal, F., & Sullivan, J. D. 1981, J. Geophys. Res., 86, 8447, doi: 10.1029/JA086iA10p08447

Barber, R. J., Tennyson, J., Harris, G. J., & Tolchenov, R. N. 2006, MNRAS, 368, 1087, doi: 10.1111/j.1365-2966.2006.10184.x

Barnes, J. R., Collier Cameron, A., James, D. J., & Donati, J. F. 2000, MNRAS, 314, 162, doi: 10.1046/j.1365-8711.2000.03237.x

Berry, I. D., Owocki, S. P., Shultz, M. E., & ud-Doula, A. 2022, MNRAS, 511, 4815, doi: 10.1093/mnras/stac322

Bhatti, W., Bouma, L., Joshua, et al. 2021, waqasbhatti/astrobase: astrobase v0.5.3, v0.5.3, Zenodo, Zenodo, doi: 10.5281/zenodo.1011188

Bildsten, L., Brown, E. F., Matzner, C. D., & Ushomirsky, G. 1997, ApJ, 482, 442, doi: 10.1086/304151

Bochanski, J. J., West, A. A., Hawley, S. L., & Covey, K. R. 2007, AJ, 133, 531, doi: 10.1086/510240

Bouma, L. G., Jayaraman, R., Rappaport, S., et al. 2024, AJ, 167, 38, doi: 10.3847/1538-3881/ad0c4c

Bouma, L. G., Winn, J. N., Ricker, G. R., et al. 2020, AJ, 160, 86, doi: 10.3847/1538-3881/ab9e73

Briceño, C., Calvet, N., Hernández, J., et al. 2019, AJ, 157, 85, doi: 10.3847/1538-3881/aaf79b

Brown, B. P., Oishi, J. S., Vasil, G. M., Lecoanet, D., & Burns, K. J. 2020, ApJL, 902, L3, doi: 10.3847/2041-8213/abb9a4

Burke, C. J., Pinsonneault, M. H., & Sills, A. 2004, ApJ, 604, 272, doi: 10.1086/381242

Callingham, J. R., Vedantham, H. K., Shimwell, T. W., et al. 2021, Nature Astronomy, 5, 1233, doi: 10.1038/s41550-021-01483-0

Cang, T. Q., Petit, P., Donati, J. F., & Folsom, C. P. 2021, A&A, 654, A42, doi: 10.1051/0004-6361/202141975

Cang, T. Q., Petit, P., Donati, J. F., et al. 2020, A&A, 643, A39, doi: 10.1051/0004-6361/202037693

Chen, Y., Girardi, L., Bressan, A., et al. 2014, MNRAS, 444, 2525, doi: 10.1093/mnras/stu1605

Chubak, C., Marcy, G., Fischer, D. A., et al. 2012, arXiv e-prints, arXiv:1207.6212, doi: 10.48550/arXiv.1207.6212

Collier Cameron, A., & Robinson, R. D. 1989, MNRAS, 236, 57, doi: 10.1093/mnras/236.1.57

Collier Cameron, A., & Woods, J. A. 1992, MNRAS, 258, 360, doi: 10.1093/mnras/258.2.360

Croll, B., Rappaport, S., DeVore, J., et al. 2014, ApJ, 786, 100, doi: 10.1088/0004-637X/786/2/100

Cutri, R. M., Wright, E. L., Conrow, T., et al. 2021, VizieR Online Data Catalog, II/328

Dahm, S. E. 2015, ApJ, 813, 108, doi: 10.1088/0004-637X/813/2/108

Daley-Yates, S., & Jardine, M. M. 2024, MNRAS, 534, 621, doi: 10.1093/mnras/stae2131

Donati, J. F., & Landstreet, J. D. 2009, ARA&A, 47, 333, doi: 10.1146/annurev-astro-082708-101833

Donati, J. F., Mengel, M., Carter, B. D., et al. 2000, MNRAS, 316, 699, doi: 10.1046/j.1365-8711.2000.03570.x

Douglas, S. T., Curtis, J. L., Agüeros, M. A., et al. 2019, ApJ, 879, 100, doi: 10.3847/1538-4357/ab2468

Draine, B. T. 2011, Physics of the Interstellar and Intergalactic Medium

Dressing, C. D., & Charbonneau, D. 2015, ApJ, 807, 45, doi: 10.1088/0004-637X/807/1/45

Dunstone, N. J., Collier Cameron, A., Barnes, J. R., & Jardine, M. 2006, MNRAS, 373, 1308, doi: 10.1111/j.1365-2966.2006.11128.x

Feiden, G. A. 2016, A&A, 593, A99, doi: 10.1051/0004-6361/201527613

Feinstein, A. D., Montet, B. T., Ansdell, M., et al. 2020, AJ, 160, 219, doi: 10.3847/1538-3881/abac0a

France, K., Loyd, R. O. P., Youngblood, A., et al. 2016, ApJ, 820, 89, doi: 10.3847/0004-637X/820/2/89

Gagné, J., Mamajek, E. E., Malo, L., et al. 2018, ApJ, 856, 23, doi: 10.3847/1538-4357/aaae09

Gaia Collaboration, Brown, A. G. A., Vallenari, A., et al. 2018, A&A, 616, A1, doi: 10.1051/0004-6361/201833051

Gaia Collaboration, Vallenari, A., Brown, A. G. A., et al. 2023, A&A, 674, A1, doi: 10.1051/0004-6361/202243940

Gaidos, E., Mann, A. W., Rojas-Ayala, B., et al. 2022, MNRAS, 514, 1386, doi: 10.1093/mnras/stac1433

Gray, D. F. 2008, The Observation and Analysis of Stellar Photospheres

Green, G. M., Schlafly, E., Zucker, C., Speagle, J. S., & Finkbeiner, D. 2019, ApJ, 887, 93, doi: 10.3847/1538-4357/ab5362

Günther, M. N., Berardo, D. A., Ducrot, E., et al. 2022, AJ, 163, 144, doi: 10.3847/1538-3881/ac503c

Haisch, Jr., K. E., Lada, E. A., & Lada, C. J. 2001, ApJL, 553, L153, doi: 10.1086/320685

Hayashi, C., & Nakano, T. 1963, Progress of Theoretical Physics, 30, 460, doi: 10.1143/PTP.30.460

Howard, A. W., Johnson, J. A., Marcy, G. W., et al. 2010, ApJ, 721, 1467, doi: 10.1088/0004-637X/721/2/1467

Hummer, D. G., & Storey, P. J. 1987, MNRAS, 224, 801, doi: 10.1093/mnras/224.3.801

Hunt, E. L., & Reffert, S. 2024, A&A, 686, A42, doi: 10.1051/0004-6361/202348662

Hunter, J. D., et al. 2007, Computing in science and engineering, 9, 90

Husser, T. O., Wende-von Berg, S., Dreizler, S., et al. 2013, A&A, 553, A6, doi: 10.1051/0004-6361/201219058

Jeffries, R. D., Jackson, R. J., Wright, N. J., et al. 2023, MNRAS, 523, 802, doi: 10.1093/mnras/stad1293

Jenkins, J. M., Twicken, J. D., McCauliff, S., et al. 2016, in Society of Photo-Optical Instrumentation Engineers (SPIE) Conference Series, Vol. 9913, Software and Cyberinfrastructure for Astronomy IV, ed. G. Chiozzi & J. C. Guzman, 99133E, doi: 10.1117/12.2233418

Johns-Krull, C. M., Prato, L., McLane, J. N., et al. 2016, ApJ, 830, 15, doi: 10.3847/0004-637X/830/1/15

Kanodia, S., & Wright, J. 2018, Research Notes of the American Astronomical Society, 2, 4, doi: 10.3847/2515-5172/aaa4b7

Kaur, S., Viganò, D., Béjar, V. J. S., et al. 2024, A&A, 691, L17, doi: 10.1051/0004-6361/202452037

Kochukhov, O. 2021, A&A Rv, 29, 1, doi: 10.1007/s00159-020-00130-3

Kochukhov, O., Lundin, A., Romanyuk, I., & Kudryavtsev, D. 2011, ApJ, 726, 24, doi: 10.1088/0004-637X/726/1/24

Koen, C. 2021, A&A, 647, L1, doi: 10.1051/0004-6361/202140400

—. 2023, MNRAS, 518, 2921, doi: 10.1093/mnras/stac3276

Krtička, J., Mikulášek, Z., Kurfürst, P., & Oksala, M. E. 2022, A&A, 659, A37, doi: 10.1051/0004-6361/202141997

Lee, J., Song, I., & Murphy, S. 2020, MNRAS, 494, 62, doi: 10.1093/mnras/staa689

Leitzinger, M., Odert, P., Zaqarashvili, T. V., et al. 2016, MNRAS, 463, 965, doi: 10.1093/mnras/stw1922

Marigo, P., Girardi, L., Bressan, A., et al. 2008, A&A, 482, 883, doi: 10.1051/0004-6361:20078467

Mikulášek, Z., Krtička, J., Shultz, M. E., et al. 2020, in Stellar Magnetism: A Workshop in Honour of the Career and Contributions of John D. Landstreet, ed. G. Wade, E. Alecian, D. Bohlender, & A. Sigut, Vol. 11, 46–53, doi: 10.48550/arXiv.1912.04121

Pecaut, M. J., & Mamajek, E. E. 2013, ApJS, 208, 9, doi: 10.1088/0067-0049/208/1/9

—. 2016, MNRAS, 461, 794, doi: 10.1093/mnras/stw1300

Petit, V., Owocki, S. P., Wade, G. A., et al. 2013, MNRAS, 429, 398, doi: 10.1093/mnras/sts344

Pfalzner, S., & Dincer, F. 2024, ApJ, 963, 122, doi: 10.3847/1538-4357/ad1bef

Phan, D., Pradhan, N., & Jankowiak, M. 2019, arXiv e-prints, arXiv:1912.11554, doi: 10.48550/arXiv.1912.11554

Popinchalk, M., Faherty, J. K., Curtis, J. L., et al. 2023, ApJ, 945, 114, doi: 10.3847/1538-4357/acb055

Rackham, B. V., Apai, D., & Giampapa, M. S. 2018, ApJ, 853, 122, doi: 10.3847/1538-4357/aaa08c

Rampalli, R., Agüeros, M. A., Curtis, J. L., et al. 2021, ApJ, 921, 167, doi: 10.3847/1538-4357/ac0c1e

Randich, S., Tognelli, E., Jackson, R., et al. 2018, A&A, 612, A99, doi: 10.1051/0004-6361/201731738

Ratzenböck, S., Großschedl, J. E., Möller, T., et al. 2023, A&A, 677, A59, doi: 10.1051/0004-6361/202243690

Reach, W. T., Lisse, C., von Hippel, T., & Mullally, F. 2009, ApJ, 693, 697, doi: 10.1088/0004-637X/693/1/697

Rebull, L. M., Stauffer, J. R., Cody, A. M., et al. 2020, AJ, 159, 273, doi: 10.3847/1538-3881/ab893c

—. 2018, AJ, 155, 196, doi: 10.3847/1538-3881/aab605

Rebull, L. M., Stauffer, J. R., Hillenbrand, L. A., et al. 2017, ApJ, 839, 92, doi: 10.3847/1538-4357/aa6aa4

—. 2022, AJ, 164, 80, doi: 10.3847/1538-3881/ac75f1

Rebull, L. M., Stauffer, J. R., Bouvier, J., et al. 2016, AJ, 152, 114, doi: 10.3847/0004-6256/152/5/114

Redfield, S., Batalha, N., Benneke, B., et al. 2024, arXiv e-prints, arXiv:2404.02932, doi: 10.48550/arXiv.2404.02932

Reiners, A., Shulyak, D., Käpylä, P. J., et al. 2022, A&A, 662, A41, doi: 10.1051/0004-6361/202243251

Ribas, Á., Bouy, H., & Merín, B. 2015, A&A, 576, A52, doi: 10.1051/0004-6361/201424846

Ricker, G. R., Winn, J. N., Vanderspek, R., et al. 2015, Journal of Astronomical Telescopes, Instruments, and Systems, 1, 014003, doi: 10.1117/1.JATIS.1.1.014003

Rickman, H. 1989, Advances in Space Research, 9, 59, doi: 10.1016/0273-1177(89)90241-X

Sanderson, H., Jardine, M., Collier Cameron, A., Morin, J., & Donati, J. F. 2023, MNRAS, 518, 4734, doi: 10.1093/mnras/stac3302

Shultz, M. E., Wade, G. A., Rivinius, T., et al. 2018, MNRAS, 475, 5144, doi: 10.1093/mnras/sty103

Silverberg, S. M., Wisniewski, J. P., Kuchner, M. J., et al. 2020, ApJ, 890, 106, doi: 10.3847/1538-4357/ab68e6

Skelly, M. B., Unruh, Y. C., Collier Cameron, A., et al. 2008, MNRAS, 385, 708, doi: 10.1111/j.1365-2966.2008.12917.x

Skrutskie, M. F., Cutri, R. M., Stiening, R., et al. 2006, AJ, 131, 1163, doi: 10.1086/498708

Stassun, K. G., Oelkers, R. J., Paegert, M., et al. 2019, AJ, 158, 138, doi: 10.3847/1538-3881/ab3467

Stauffer, J., Collier Cameron, A., Jardine, M., et al. 2017, AJ, 153, 152, doi: 10.3847/1538-3881/aa5eb9

Stauffer, J., Rebull, L., David, T. J., et al. 2018, AJ, 155, 63, doi: 10.3847/1538-3881/aaa19d

Stauffer, J., Rebull, L. M., Jardine, M., et al. 2021, AJ, 161, 60, doi: 10.3847/1538-3881/abc7c6

Stellingwerf, R. F. 1978, ApJ, 224, 953, doi: 10.1086/156444

Tanimoto, Y., Yamashita, T., Ui, T., et al. 2020, PASJ, 72, 23, doi: 10.1093/pasj/psz145

Tofflemire, B. M., Rizzuto, A. C., Newton, E. R., et al. 2021, AJ, 161, 171, doi: 10.3847/1538-3881/abdf53

Tokovinin, A., & Briceño, C. 2018, AJ, 156, 138, doi: 10.3847/1538-3881/aad906

Townsend, R. H. D. 2008, MNRAS, 389, 559, doi: 10.1111/j.1365-2966.2008.13462.x

Townsend, R. H. D., & Owocki, S. P. 2005, MNRAS, 357, 251, doi: 10.1111/j.1365-2966.2005.08642.x

TRAPPIST-1 JWST Community Initiative, de Wit, J., Doyon, R., et al. 2024, Nature Astronomy, 8, 810, doi: 10.1038/s41550-024-02298-5

Van Der Walt, S., Colbert, S. C., & Varoquaux, G. 2011, Computing in Science & Engineering, 13, 22

van Eyken, J. C., Ciardi, D. R., von Braun, K., et al. 2012, ApJ, 755, 42, doi: 10.1088/0004-637X/755/1/42

Vial, J.-C., & Engvold, O. 2015, Astrophysics and Space Science Library, Vol. 415, Solar Prominences, doi: 10.1007/978-3-319-10416-4

Vines, J. I., & Jenkins, J. S. 2022, MNRAS, 513, 2719, doi: 10.1093/mnras/stac956

Virtanen, P., Gommers, R., Oliphant, T. E., et al. 2020, Nature Methods, 17, 261, doi: 10.1038/s41592-019-0686-2

Virtanen, P., Gommers, R., Oliphant, T. E., et al. 2020, Nature Methods, 17, 261, doi: 10.1038/s41592-019-0686-2

Vogt, S. S., Allen, S. L., Bigelow, B. C., et al. 1994, SPIE Conference Series, ed. D. L. Crawford & E. R. Craine, Vol. 2198

Waugh, R. F. P., & Jardine, M. M. 2022, MNRAS, 514, 5465, doi: 10.1093/mnras/stac1698

Winters, J. G., Henry, T. J., Jao, W.-C., et al. 2019, AJ, 157, 216, doi: 10.3847/1538-3881/ab05dc

Wood, M. L., Mann, A. W., Barber, M. G., et al. 2023, AJ, 165, 85, doi: 10.3847/1538-3881/aca8fc

York, D. G., Adelman, J., Anderson, John E., J., et al. 2000, AJ, 120, 1579, doi: 10.1086/301513

Zhan, Z., Günther, M. N., Rappaport, S., et al. 2019, ApJ, 876, 127, doi: 10.3847/1538-4357/ab158c